



City Research Online

City, University of London Institutional Repository

Citation: Wang, J., Ma, Q., Yang, Z., Gao, J. & Wu, G. (2022). Two types of wave-current interactions and their effects on extreme waves in directional seas. *Ocean Engineering*, 266(1), 112637. doi: 10.1016/j.oceaneng.2022.112637

This is the accepted version of the paper.

This version of the publication may differ from the final published version.

Permanent repository link: <https://openaccess.city.ac.uk/id/eprint/30060/>

Link to published version: <https://doi.org/10.1016/j.oceaneng.2022.112637>

Copyright: City Research Online aims to make research outputs of City, University of London available to a wider audience. Copyright and Moral Rights remain with the author(s) and/or copyright holders. URLs from City Research Online may be freely distributed and linked to.

Reuse: Copies of full items can be used for personal research or study, educational, or not-for-profit purposes without prior permission or charge. Provided that the authors, title and full bibliographic details are credited, a hyperlink and/or URL is given for the original metadata page and the content is not changed in any way.

City Research Online:

<http://openaccess.city.ac.uk/>

publications@city.ac.uk

Two Types of Wave-Current Interactions and Their Effects on Extreme Waves in Directional Seas

Jinghua Wang¹, Qingwei Ma², Zhengtong Yang^{*,3}, Junliang Gao⁴, Guoxiang Wu⁵

¹Department of Civil and Environmental Engineering, The Hong Kong Polytechnic University, Hong Kong

²School of Mathematics, Computer Science and Engineering, City, University of London, United Kingdom

³Technology Centre for Offshore and Marine, Singapore (TCOMS), Singapore

⁴School of Naval Architecture and Ocean Engineering, Jiangsu University of Science and Technology, China

⁵School of Engineering, Ocean University of China, China

Abstract

The nonlinear wave-current interactions can influence and change extreme wave probability, spectral characteristics, and average shape of extreme waves significantly (Wang, J., Ma, Q. W., & Yan, S. (2021). On Extreme Waves in Directional Seas with Presence of Oblique Current. *Applied Ocean Research*, 112, pp. 102586). There are different scenarios of wave-wave interactions in reality. This study identifies two types of wave-current interactions: Type-I (waves propagating from current-negligible region to current-significant region) and Type-II (waves propagating from current-significant region to current-negligible region). The impacts of the two types of wave-current interactions on extreme wave probability and the spectral properties will be investigated by using fully nonlinear potential flow model. The numerical results reveal that the changes

* Correspondence to: 12 Prince George's Park, 118411, Singapore

E-mail address: yang_zhengtong@tcoms.sg

18 in extreme wave probability and spectral properties due to Type-I are more evident than those induced by Type-
19 II.

20 **Keywords:** Rogue waves; Exceedance probability; Nonlinear wave spectra; Phase-resolved simulations. Fully
21 nonlinear potential theory.

22 **1 Introduction**

23 Extreme waves in the ocean are responsible for causing substantial damages to ocean engineering applications
24 and threatening human's maritime activities. They can emerge without the external forcing, and their physical
25 mechanisms are explained by two competing hypotheses: i) dispersive focusing of second-order non-resonant
26 harmonic waves, and ii) nonlinear quasi-resonant wave-wave interactions (Fedele, et al., 2016). They exhibit
27 highly asymmetric cross-sectional profile in main wave direction and often appear in a sea state with kurtosis
28 greater than 3, high tail values at probability distribution, and their directional spectra feature widened bandwidth
29 and downshifted spectral peak (comparing with those predicted based on the linear theories) (Dysthe, et al., 2008;
30 Kharif, et al., 2009; Adcock & Taylor, 2014). In narrow-banded seas, their statistics can be well described by the
31 third-order Tayfun distribution and dynamic excess kurtosis (Janssen, 2003; 2009; Mori & Janssen, 2006; Tayfun
32 & Fedele, 2007; Onorato, et al., 2008), albeit the increase of directionality can suppress the occurrences of
33 extreme waves (Janssen & Bidlot, 2009; Fedele, 2015) and the second-order theories becomes sufficient (Fedele,
34 et al., 2016). Meanwhile, with increased flow rate, the growth rate of the resonating waves due to the third-order
35 resonance can also be suppressed. This detuning effect was shown to be caused by the variation of the current
36 field (Waseda, et al., 2015).

37 In addition, the interactions between waves and current have been widely recognized for provoking extreme
38 waves (Lavrenov, 1998; White & Fornberg, 1998; Lavrenov & Porubov, 2006; Cattrell, et al., 2018). In general,
39 the presence of current can be responsible for (i) amplifying wave height around a caustic by refraction and
40 nonlinear wave-current interactions (White & Fornberg, 1998; Janssen & Herbers, 2009; Moreira & Peregrine,
41 2012) and (ii) triggering the quasi-resonant wave-wave interactions (Bakhanov, et al., 1996; Stocker & Peregrine,
42 1999; Nwogu, 2009; Toffoli, et al., 2011; Ruban, 2012; Ma, et al., 2013; Manolidis, et al., 2019). The latter is
43 also associated with vertically shearing current (Choi, 2009; Thomas, et al., 2012; Touboul & Kharif, 2016;
44 Guyenne, 2017; Kharif, et al., 2017; Liao, et al., 2017). Very recently, the study using fully nonlinear simulations
45 has revealed that the nonlinear wave-current interaction can induce the enhanced exceedance probability at tail,
46 amplified kurtosis, increased directionality, reduced spectral energy (significant height), lessened spectral peak
47 downshift, and the highly distorted asymmetric extreme wave profiles (Wang, et al., 2021). The formation of
48 extreme waves in random seas with presence of current has been comprehensively reviewed in Wang, et al.
49 (2021), so it will not be repeated hereby.

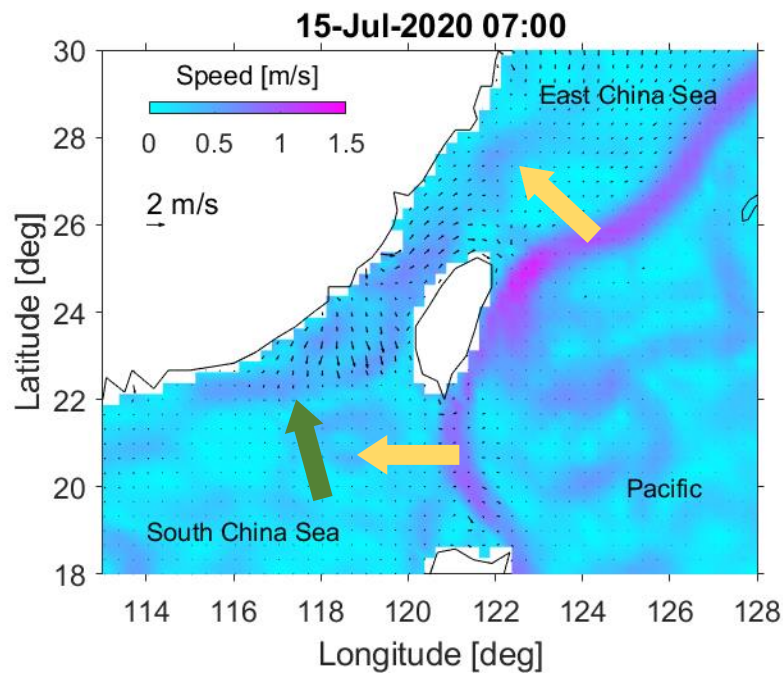
50 The above studies have focused on the scenario that the wave and current co-exist in the same region. This
51 corresponds to the situation that waves propagate from relatively deep-water area with negligible current towards
52 a nearshore region where the along-shore current becomes stronger. Depending on the coastline configuration
53 and wind wave/swell direction, the angle between the main wave and current flow direction can be oblique or
54 opposed, for instance, the Agulhas current region off South Africa (Lavrenov, 1998). It can also happen when
55 waves arrive at the coastal regions at the ebb phase of tidal current, e.g., the northern part of the South China
56 shown in Figure 1 (wave propagations are represented by the thick green arrow). This type of wave-current

57 interaction is named as Type-I WCI hereafter.

58 Another scenario is that the wave-current interaction takes place in a region far away, and subsequently waves
59 arrive at the location of interests with very weak or negligible current. This type of wave-current interaction
60 (referred as Type-II WCI hereafter) is often observed in a zone with close proximity to a meandering current.
61 Meanwhile, the waves are mild in steepness and the gradient of the current velocity is small, therefore the
62 interactions between waves and current can be described by linear theories. After escaping from the region, the
63 waves are developed and then propagate into a current free zone. For example, as shown in Figure 1, waves may
64 travel to or be generated in the region of Kuroshio current. Then the waves enter South China Sea from the
65 Pacific Ocean via Luzon Strait, as well as the waves approaching the East China Sea through edge of the shelf
66 in north Taiwan (wave propagations are highlighted by the thick yellow arrows), where the current becomes very
67 weak and negligible.

68 The strength of the nonlinearities of a random wave field due to Type-I WCI are mainly associated with the
69 magnitude of wave steepness and current gradient, meanwhile the wave steepness amplification/reduction due
70 to the presence of current depends on the flow speed and direction (more details will be given in section 2.2).
71 Therefore, the nonlinear characteristics of the wave field are influenced by both the nonlinear wave-wave
72 interactions (associated with wave steepness) and wave-current interactions (associated with wave steepness and
73 current gradient). In contrast to the Type-I with coexistence of waves and current, only the nonlinear wave-wave
74 interactions (associated with wave steepness) in Type-II will play key roles in producing nonlinear wave
75 properties. The Type-II WCI is rarely considered as far as we know. However, it cannot be rolled out that the
76 obtained wave spectra at two different locations due to such two mechanisms can be similar. It gives rise to the

77 scientific question that whether the resulted nonlinear wave properties and corresponding mechanism will be
78 different between the two types of wave-current interactions. This constitutes the main driver of this study and
79 gaining insights of this question can contribute to clarifying the mechanisms of ocean extreme waves under the
80 action of current. The conclusions obtained are crucial for predicting and quantifying such extreme events in the
81 regions of interests.



82
83 Figure 1. Geographic illustration of the two types of wave-current interaction mechanisms. Graded color
84 represents the strength of the southwesterly Kuroshio Current. Thin black arrows denote the strength and
85 direction of the tidal current on the indicated date. Colored thick arrows indicate the directions of wind
86 waves/swells. White color is the land mask with China mainland in the northwest, Taiwan in the middle and
87 Philippine at the bottom. The tidal current velocity is reconstructed based on the FES2014 release (Lyard, et
88 al., 2021) and the data of geostrophic current velocities are downloaded from ECMWF website (ECMWF,

89 2018).

90

91 To answer the question, this study investigates two groups of problems by using fully nonlinear and phase-
92 resolved approach on a large spatiotemporal scale. Specifically:

93 **Group (I):** the directional waves without the current are generated in a zone, and then they propagate from
94 the current-free zone to the current-established region.

95 **Group (II):** the directional waves are generated by using a linear current-modified wave spectrum, and
96 then they propagate in a current-free zone.

97 Hence, Group (I) will account for the fully nonlinear wave-current (including fully nonlinear wave-wave)
98 interactions to model the Type-I WCI. Whereas to represent the Type-II WCI, Group (II) simulations only
99 consider the linear wave-current interactions in the wave spectrum, while the nonlinear wave characteristics will
100 automatically develop due to fully nonlinear wave-wave interactions alone. By comparing the results obtained
101 from the two groups, this study will identify and emphasize the differences in nonlinear wave properties due to
102 two types of WCI. The focus of the study will be on two current-induced non-Gaussian properties: one is the
103 extreme wave probability, in particular the exceedance probability of large wave crests, and the second is the
104 spectral properties including the changes of spectral shapes and spectral peak downshift.

105 **2 Methodologies**

106 To numerically reproduce the sea states with sufficient accuracy on simulating fully nonlinear wave-wave and

107 wave-current interactions, the Enhanced Spectral Boundary Integral (ESBI) method is employed. Note that this
108 study has assumed that the horizontal velocity of the current is independent of the vertical coordinate, which is
109 a reasonable approximation to the current field in deep water where the characteristic time and length scale of
110 the oceanic current is large compared with wind-waves (Longuet-Higgins & Stewart, 1961; Peregrine, 1976).
111 Nevertheless, the variation of its vertical structure can become important when considering wind driven surface
112 current in finite-depth or shallow water (Nwogu, 2009), which however is not the focus of this study. On the
113 other hand, to generate waves in the Group (II) simulations with the current-modified linear wave spectrum, the
114 formulations of Lavrenov (1998; 2003) is adopted. Details about the ESBI model and the current-modified
115 spectrum are given in this section.

116 **2.1 Fully nonlinear simulations**

117 In this study, the Enhanced Spectral Boundary Integral (ESBI) method for modelling fully nonlinear wave-wave
118 and wave-current interactions (Wang & Ma, 2015; Wang, et al., 2018) is employed. The details of the method
119 are well documented in Wang & Ma (2015) and Wang, et al. (2018), and only some key equations are briefed
120 here for completeness.

121 All the variables used in the ESBI have been non-dimensionalized, e.g., those in length (X, Z) are multiplied
122 by peak wavenumber k_p , time T by peak frequency ω_p , velocity potential by k_p^2/ω_p and velocity by k_p/ω_p ,
123 while the dispersion relation is given by $\omega_p = \sqrt{gk_p}$. The overall free surface elevation and flow velocity can
124 be split into two parts, i.e.,

$$\zeta = \bar{\eta} + \eta \quad (1)$$

$$\vec{U} = \vec{U} + (\nabla, \partial_z)\phi \quad (2)$$

125 where $\nabla = (\partial_x, \partial_y)$ is the horizontal gradient operator, $\vec{U} = (U, W)$ and $\bar{\eta}$ are the current velocity and current
 126 induced surface elevation without waves, respectively; ϕ and η are the velocity potential and deflection of the
 127 free surface involving the contributions from both waves and wave-current interactions. Using the free surface
 128 boundary conditions, the prognostic equation can be written as

$$\partial_T \vec{M} + A \vec{M} = \vec{N} \quad (3)$$

129 where

$$\vec{M} = \begin{pmatrix} KF\{\eta\} \\ K\Omega F\{\tilde{\phi}\} \end{pmatrix}, \quad A = \begin{bmatrix} 0 & -\Omega \\ \Omega & 0 \end{bmatrix} \quad \text{and} \quad \vec{N} = \begin{pmatrix} K(\Phi - \mu) \\ K\Omega(\Psi - \psi) \end{pmatrix}, \quad (4)$$

130 and $\tilde{\phi}$ denotes the velocity potential at the surface; $F\{*\}$ and $F^{-1}\{*\}$ are the Fourier and the inverse
 131 transform, respectively; $K = |\mathbf{K}|$ is the wavenumber; $\Omega = \sqrt{K}$ is the frequency; and Φ and Ψ are nonlinear
 132 terms due to fully nonlinear wave-wave interactions, while μ and ψ represent the fully nonlinear wave-current
 133 interactions.

134 Eq.(3) will be used to update the free surface and velocity potential in time domain by using the fifth-order
 135 Runge-Kutta method with adaptive time step. An energy dissipation model that has been comprehensively
 136 verified (Xiao, et al., 2013) is also introduced to suppress breaking waves and it is applied only when wave
 137 steepness becomes extremely large. The formulations for (Φ, Ψ, μ, ψ) can be found in the Appendix.
 138 Validations of the model are also presented in Wang, et al. (2018), but details are omitted hereby for simplicity.

139 **2.2 Current-modified directional wave spectrum based on linear theory**

140 From the perspective of wave action conservation, the linear current-modified directional wave spectrum can be
 141 derived as (Lavrenov, 1998; 2003)

$$\frac{\hat{S}(\omega, \theta)}{\hat{S}_0(\omega, \theta_0)} = \frac{16}{\sqrt{1 + u' \cos(\varphi - \theta)} [1 + \sqrt{1 + u' \cos(\varphi - \theta)}]^4} \quad (5)$$

142 where $\hat{S}(\omega, \theta)$ and $\hat{S}_0(\omega, \theta_0)$ represent the directional spectra with and without current, respectively, θ_0 and
 143 θ denote the direction of wave propagation before and after encountering the current as shown in Figure 2. In
 144 Eq.(5), $u' = 4\omega u/g$ where $u = |\mathbf{u}|$ is the magnitude of the current speed, g is the gravitational acceleration,
 145 and ω is the frequency measured in an immovable coordinate system, which connects with the frequency σ
 146 measured in the moving frame through

$$\omega = \sigma + \mathbf{u} \cdot \mathbf{k} \quad (6)$$

147 where $\mathbf{u} = (u \cos \varphi, u \sin \varphi)$ and φ is the incident angle of the current. Eq. (5) is consistent with that derived
 148 by Nwogu (2009) in terms of wave amplitude. For unidirectional waves with opposed current, Eq. (5) reduces
 149 to that obtained by Huang, et al. (1972). Correspondingly, the shift of peak wavenumber can be obtained as

$$\frac{k_p}{k_{p0}} = \frac{4}{(1 + \sqrt{1 + u' \cos \varphi})^2} \quad (7)$$

150 with k_{p0} being the peak wavenumber in the current-free zone.

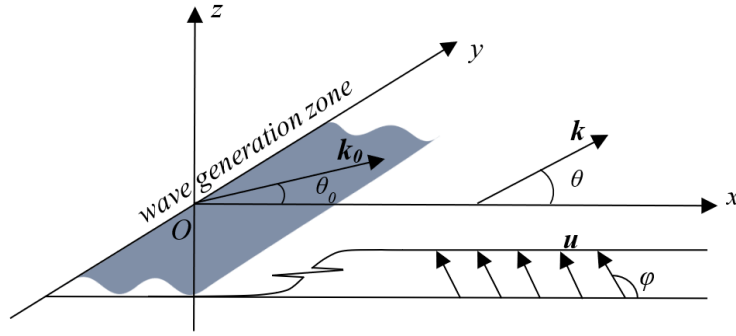
151 Note that following Longuet-Higgins & Stewart (1961), Eq. (5) can also be derived by using Eqs. (3) and (4)
 152 and retaining the terms of first order in wave steepness $O(\varepsilon)$, current gradient $O(\beta = \sigma^{-1} \partial_x u)$ and their

153 products $O(\varepsilon\beta)$. Therefore, it considers only the linear (leading order) wave-current interactions. Any higher-
154 order nonlinear terms in the magnitudes greater than $O(\varepsilon^2, \beta^2, \varepsilon^m \beta^n)$, where $m + n > 2$, are neglected,
155 including the terms represents the nonlinear wave-current interactions.

156 It is reiterated that the nonlinear statistical and spectral properties of a random sea can be due to nonlinear wave-
157 wave interactions alone, or through the nonlinear wave-current interactions (including the nonlinear wave-wave
158 interactions). That is being said, the role of the nonlinear effects of the current is unclear in producing the resulted
159 nonlinear wave characteristics when waves of large steepness are superimposed on current. Therefore, the
160 purpose of this study is to quantify the additional nonlinear effects due to the current through comparing the
161 simulation results of nonlinear wave-current interactions (Type-I WCI) with those of composite linear wave-
162 current and nonlinear wave-wave interactions (Type-II WCI) on the nonlinear wave properties of interests.
163 Regarding this purpose, the current-modified spectrum $\hat{S}(\omega, \theta)$ can be obtained with the input spectrum
164 $\hat{S}_0(\omega, \theta_0)$. This spectrum $\hat{S}(\omega, \theta)$ will be used for wave generation in Group (II) simulations to consider the
165 linear wave-current effects alone. After the waves are generated from the wave generation/wavemaker zone,
166 only the fully nonlinear wave-wave interactions will be simulated with current speed set to zero.

167

168



169

170

Figure 2. Illustration of the wave-current interaction problem.

171 3 Numerical results

172 Regarding the purpose of this study, we employ a computational domain as illustrated in Figure 3. The

173 computational domain covers an area of $50L_p \times 50L_p$ and is resolved into 2048×1024 collocation points in X -

174 direction (mean wave direction) and Y -direction, respectively, where L_p is the non-dimensionalized peak

175 wavelength without current in presence. The size of domain is sufficient for the wave-current interactions to

176 fully develop, and resolution of grid size leads to converged results (Wang, et al., 2018; Wang, et al., 2021).

177 Pneumatic directional wavemaker is deployed along the Y -direction with $10L_p$ away from the left boundary, and

178 the domain in the region of $40L_p \times 50L_p$ on the right-hand side is used for collecting useful results for analysis.

179 The outgoing waves are suppressed by surrounding absorbing boundaries.

180 The JONSWAP spectrum with peak factor $\gamma = 9$, peak frequency $\omega_p = 1.17s^{-1}$ (peak wavelength $\sim 45m$) is

181 used as the initial spectrum. The spreading function of $\cos^N(\theta)$ with $N = 24$ is adopted to represent a wide

182 spreading directional spectrum (Goda, 1999). Since we are only interested in strong nonlinear effects for large

183 steepness waves, the initial wave steepness is specified as $\varepsilon_0 = (k_p H_s)_0 = 0.15$ with a cut-off frequency of $1.55\omega_p$
 184 (corresponding to 1% of the spectral peak value). Although the spectral components beyond cut-off frequency
 185 are ignored for wave generation, they will develop rapidly in the domain due to fully nonlinear wave-wave
 186 interactions (Fadaeiazar, et al., 2020).

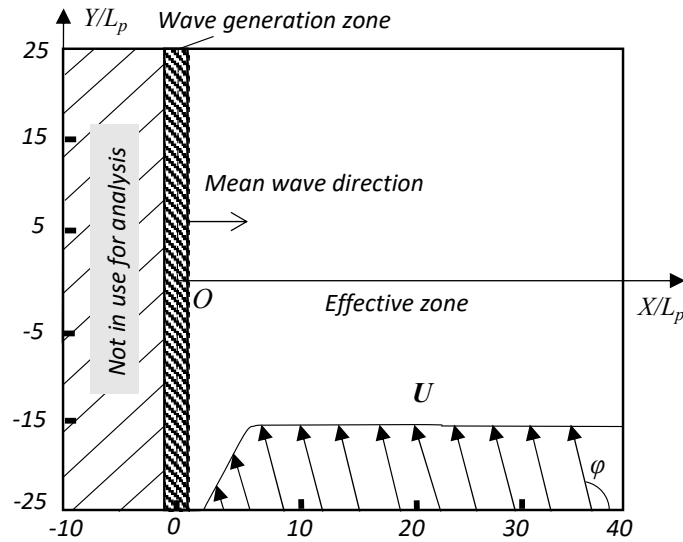
187 To model the waves propagating from a current-free zone to an established region as shown in Figure 3, we
 188 employ a current field prescribed by

$$|\mathbf{U}| = \begin{cases} 0, & X/L_p \leq 2 \\ U_m H((4 - X/L_p)/2), & 2 < X/L_p \leq 4 \\ U_m & X/L_p > 4 \end{cases} \quad (8)$$

189 which gives rise to a current gradient of $\beta \approx 0.012$. To examine the effects of different current incident angles,
 190 the values for $\varphi = 90^\circ, 110^\circ, 135^\circ, 150^\circ$ and 180° are selected, while taking $U_m = 0.3c_g$, where c_g is the
 191 wave group velocity corresponding to the peak wave period. The selection of the wave parameters and current
 192 magnitude is representative for the wave and current condition in Agulhas region (Lavrenov, 1998) and South
 193 China Sea (Fang, et al., 1998; Li, et al., 2016), etc.

194 To collect time history signal of the free surface, wave gauges are deployed in the domain spaced at $3L_p$ and
 195 $3.5L_p$ in X - and Y -direction, respectively. Note that only those in the equilibrium zone are used for analyzing
 196 the wave crest exceedance probability. Using a large number of wave gauges can overcome the insufficiency of
 197 single point observation for investigating the extreme wave ensembles (Benetazzo, et al., 2017). Note that the
 198 condition of homogeneity and independence is fulfilled after checking the wave sampling across selected wave
 199 gauges (Wang, et al., 2021), hence no additional effort is required to treat the spatiotemporal correlation (Trulsen,

200 et al., 2015).



201

202

Figure 3. Plan view of the computational domain.

203 For each case with a given initial wave steepness ε_0 and current incident angle φ , four realizations are

204 performed with different random phases. Each realization lasts for 500 peak periods. The first 100 peak periods

205 are considered as a transitional period, and the wave signals within 100~500 periods are employed for analysis,

206 which is sufficient for achieving reliable statistical analysis (Toffoli, et al., 2011; Wang, et al., 2021). In addition,

207 the wavenumber spectra are recovered from the free surface spatial distribution saved at every peak period. Some

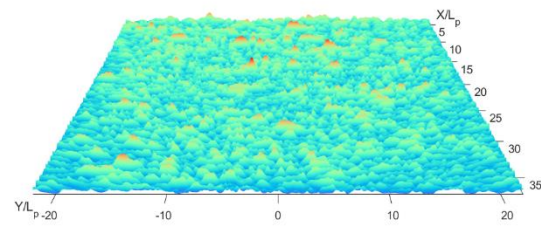
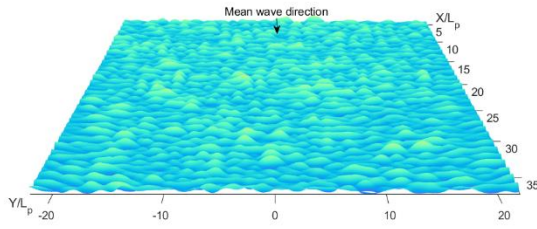
208 selected snapshots of the free surface spatial distribution at the end of the simulations are displayed in Figure 4

209 for demonstrations. It is noticed that with the effects of current, more large waves are produced in both Group

210 (I) and (II) simulations than that without current. However, the appearance of large waves in Group (I)

211 simulations is due to nonlinear wave-current interactions (Type-I WCI), whereas they are attributed to the

212 composite linear wave-current and nonlinear wave-wave interactions (Type-II WCI) in Group (II) simulations.

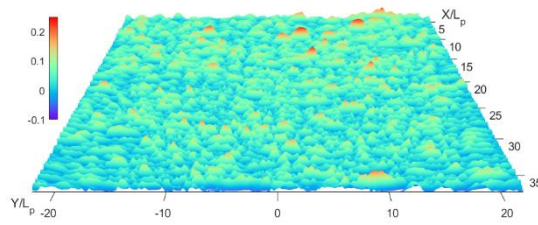


213

214

(a) No current

(b) $\varphi = 180^\circ$ (Group I)



215

216

(c) $\varphi = 180^\circ$ (Group II)

217

Figure 4. Selected free surface snapshots from simulations after 500 peak periods for $\varepsilon_0 = 0.15$.

218

219 3.1 Wave crest exceedance probability

220

Firstly, the effects of two types of WCI on the wave crest exceedance will be investigated. The exceedance

221

probability is estimated for each group of simulations, and they are displayed in Figure 5. Their differences in

222

percentage, i.e.,

$$Diff. = \frac{P^{(I)} - P^{(II)}}{P^{(I)}} \times 100\% \quad (9)$$

223 where $P^{(i)}$ with $i = \text{I or II}$ is the exceedance probability obtained based on Group (I) or (II) simulations,
224 respectively, are also calculated and presented in the figure. The figure shows that the probability of large crests
225 $\chi = H_c/H_s \geq 1.2$ (where H_c is the crest height, and this condition is often used to justify the rogue wave
226 occurrences in addition to the criterion of overall height greater than $2H_s$) is enhanced with current in presence
227 for both groups, while the enhancement is more evident for larger current incident angles. The linear theory
228 underestimates the probability of wave crest at the tail for all cases, whereas the second-order theory (Tayfun,
229 1980) is shown to be accurate only for the case without current, but it leads to underestimation for the rest cases.
230 This is consistent with the results collected in the laboratory experiments (Toffoli, et al., 2011; Toffoli, et al.,
231 2015), which implies that the numerical model employed in this study is robust and the obtained numerical
232 results are reliable. When $\varphi \geq 135^\circ$, a deceleration in growth is observed and the distributions become
233 stabilized and overlapped for both groups. However, one noticeable difference between the two groups is that at
234 $\varphi = 90^\circ$, the probability distribution in the range of $\chi < 1.1$ for Group (II) agrees with that without current,
235 whereas they are higher for Group (I). It implies that the nonlinear wave-current interactions (Type-I WCI) not
236 only enhance the probability of large waves, but also waves of moderate height when the current is perpendicular
237 to the mean wave direction. Figure 5 (c) also reveals that the probability of moderate crest heights $\chi \leq 0.5$ is
238 comparable between the two groups, while the probability for larger crests in Group (I) preserves slightly higher
239 values than that of Group (II) when incident angles $\varphi \leq 135^\circ$. The maximum difference is about 62% for $\chi =$
240 1.25 when $\varphi = 110^\circ$. However, the differences reduce with increasing incident angle. For $\varphi \geq 150^\circ$, the
241 differences between the two groups can be either positive or negative, meaning the probability of large crest in
242 Group (I) is not necessarily greater than that in Group (II). Therefore, it can be said that the Type-I WCI

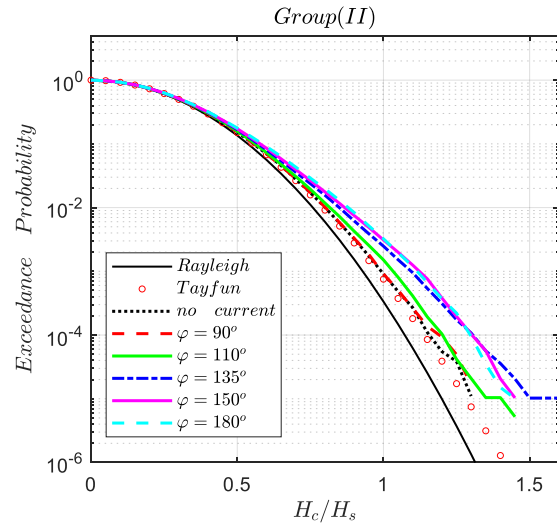
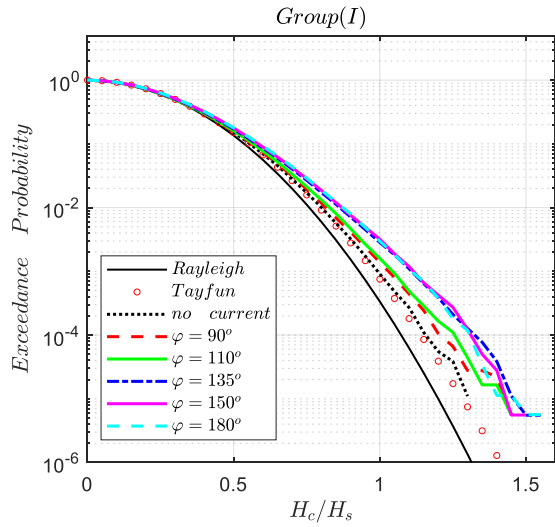
243 (nonlinear wave-current interactions) can enhance the extreme wave probability compared with the Type-II WCI
244 (composite nonlinear wave-wave interactions and linear wave-current interactions), and the enhancement is
245 more evident when the current incident angle is relatively small.

246 To quantify the enhancement of extreme wave probability due to Type-I WCI, the ratio is calculated by using
247 the formula:

$$R_p = \frac{P^{(i)}(\chi = 1.2)}{P_0(\chi = 1.2)} \quad (10)$$

248 where P_0 corresponds to that without considering current in simulations. The results are summarized and
249 presented in Figure 6. It shows that the extreme wave probability can increase by 2~8 times when current is in
250 presence. The maximum enhancement is reported at $\varphi = 150^\circ$ in all cases being studied here. The results for
251 Group (I) preserve slightly higher values than those of Group (II) meaning that the Type-I WCI is more effective
252 for enhancing the extreme wave probability. And the difference between Group (I) and (II) reaches maxima at
253 $\varphi = 135^\circ$, where the difference of the ratio is $7.01-5.67=1.34$. Whereas the difference for the cases of $\varphi = 90^\circ$
254 or 180° , i.e., when current is perpendicular or opposed to mean wave direction, is negligible. Hence it can be
255 said that under such conditions, i.e., $\varphi = 90^\circ$ or 180° , the Type-I WCI does not have strong impacts on extreme
256 wave probability, and the enhancement is mainly due to Type-II WCI.

257

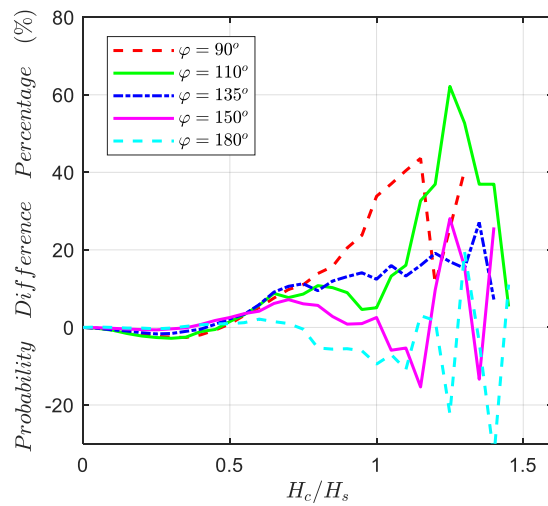


258

259

(a) Group (I)

(b) Group (II)



260

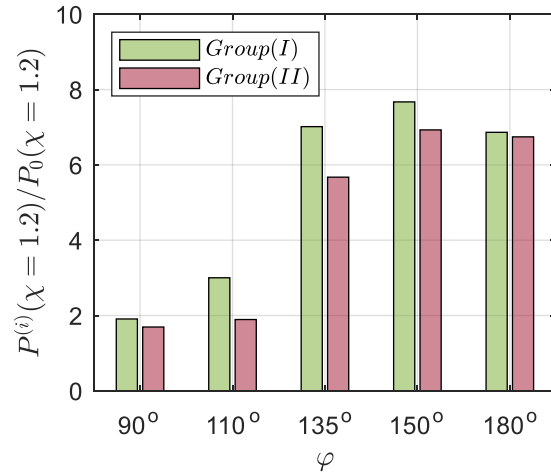
261

(c) Difference between (I) and (II)

262 Figure 5. Wave crest exceedance probability comparisons among different current incident angles. (a) Group

263 (I) accounting for fully nonlinear wave-current interactions; (b) Group (II) considering only linear wave-

264 current interactions; (c) Difference between Groups (I) and (II) in percentage.



265

266

Figure 6. Value of R_p versus current incident angle.

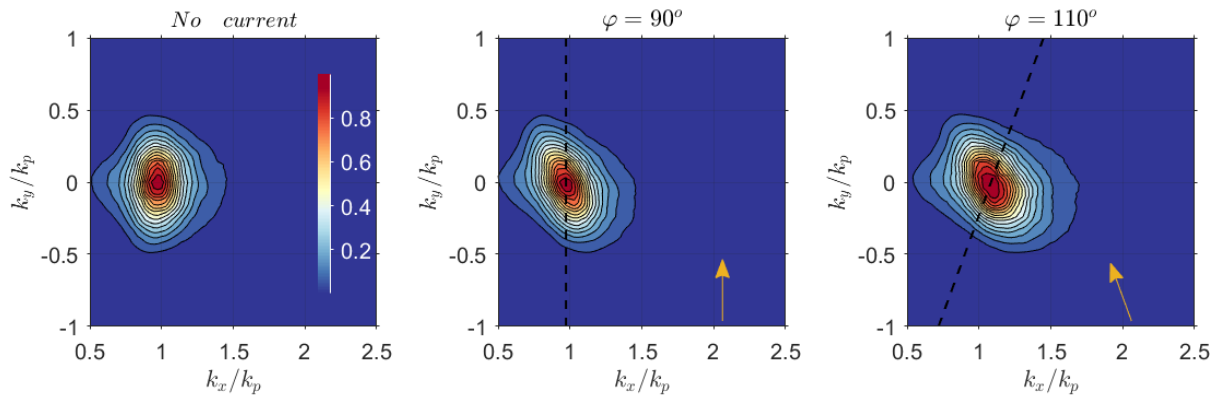
267 3.2 Wave spectral properties

268 This section discusses the changes in the spectral properties due to the two types of WCI. Here we recover the
 269 wavenumber spectra from the simulated free surface elevations and average in time and among realizations. By
 270 comparing the results of Group (I) and (II), we found that the total spectral energy and broadening of
 271 directionality are comparable and the difference is less than 5%. It implies that the Type-I WCI has marginal
 272 effects on these two spectral properties. However, the changes in spectral shape and downshift of spectral peak
 273 due to Type-I WCI is evident, which are discussed here.

274 3.2.1 Spectral shapes

275 In general, the spectra based on Group (II) simulations look similar with those obtained from Group (I)
 276 simulations (Wang, et al., 2021). Therefore, Figure 7 only displays the renormalized spectra corresponding to
 277 Group (II). For simplicity, the shapes of the linear current-modified wave spectra are not repeated here but can

278 be found in Figure 7 in Wang, et al. (2021). The figure shows that with adverse current or without current, the
 279 wave spectra are symmetrical with respect to $k_y = 0$. With oblique current in presence, wave components of
 280 $k_y < 0$ are propagating against current so they are compressed leading to an increased wavenumber; whereas
 281 those of $k_y > 0$ will be stretched resulting in a reduced wavenumber. Therefore, the obtained spectra are
 282 asymmetric with respect to $k_y = 0$. In addition, the broadening of the spectra at high wavenumber range are
 283 also observed, especially when the current incident angle is large. Therefore, it can be said that such changes in
 284 spectral shapes are mainly due to the combined effects of the Type-II WCI (composite linear wave-current and
 285 nonlinear wave-wave interactions).



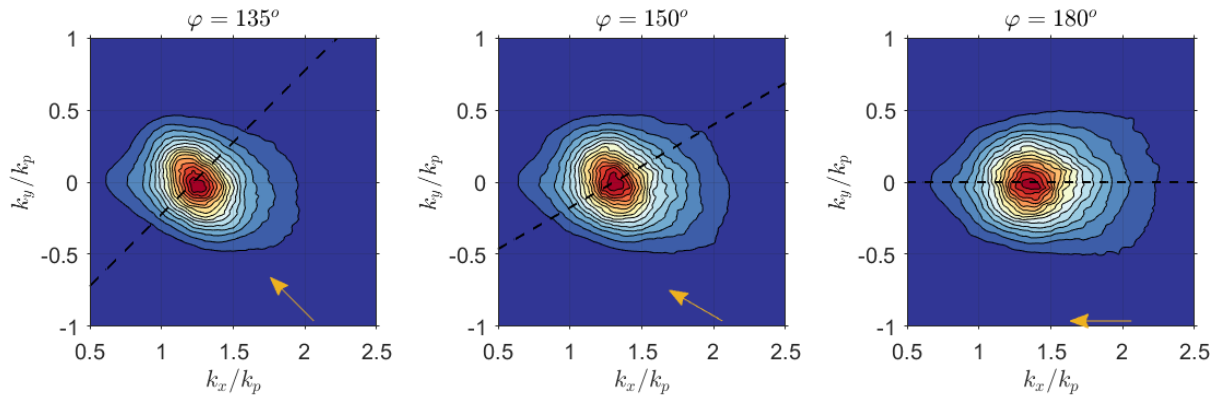
286

287

(a) No current

(b) $\varphi = 90^\circ$

(c) $\varphi = 110^\circ$



288

289 (d) $\varphi = 135^\circ$ (e) $\varphi = 150^\circ$ (f) $\varphi = 180^\circ$

290 Figure 7. Renormalized spectra based on Group (II) simulations. Arrows denote the incident current directions.

291 Black dash line indicates the section across the spectral peaks for extracting spectrum profiles.

292 Although the spectra based on Group (II) simulations are visually indistinguishable from those based on Group

293 (I) simulations, there are essential differences. To quantify these differences, the formula below is used

$$R_s = \frac{S^{(I)} - S^{(II)}}{\max\{S^{(I)}\}} \quad (11)$$

294 where $S^{(I)}$ and $S^{(II)}$ are the simulated spectra corresponding to Group (I) and (II), respectively. Based on

295 Eq.(11), it is understandable that $R_s > 0$ indicates increased spectral energy due to Type-I WCI, and *vice versa*.

296 The values for R_s are calculated for each current incident angle and they are plotted in Figure 8. In each sub-

297 figure, a straight line that divides the map of R_s into two sub-regions, and this straight line can be expressed as

$$k'_y = \cot \varphi (k'_x - k_p^{(I)}) \quad (12)$$

298 where $k_p^{(I)}$ is the peak wavenumber in X - (mean wave) direction based on Group (I) simulations. To view the

299 differences, the cross-sectional profile of the spectrum is also extracted along a straight line perpendicular to

300 Eq.(12) (the position of the cross section is marked as the black dash line in Figure 7). The extracted spectrum

301 profiles are compared and displayed in Figure 9, where the x-axis is centered at the spectral peak.

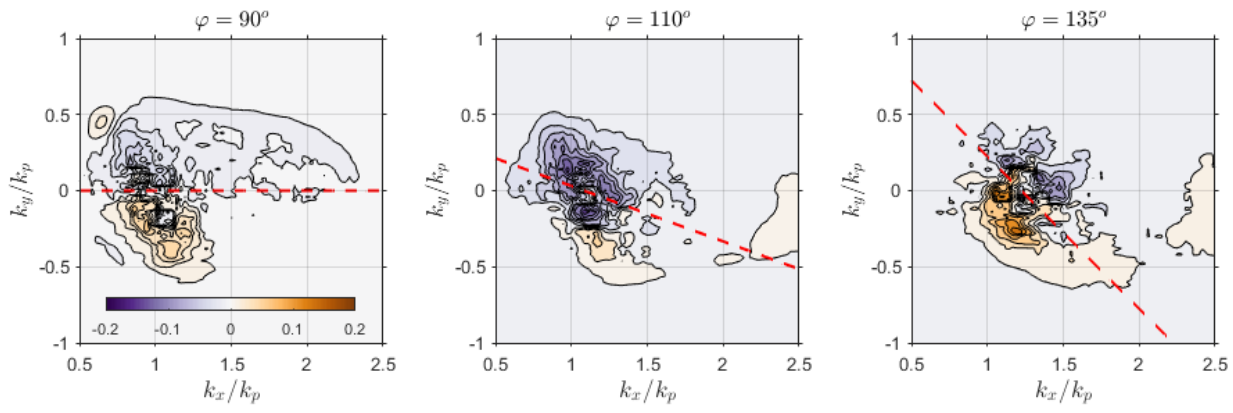
302 Figure 8 shows that for the sub-region beneath or on the left of the divider, i.e., $k_y < k'_y$ or $k_x < k'_x$, the

303 spectral energy is increased, while the spectral energy on the other side is reduced. The increase/reduction can

304 be substantial, e.g., nearly 20% among all cases being studied here. It is noted in Figure 9 that the differences of

305 spectrum sectional profiles between the two groups are more significant for relatively larger current incident

306 angles, e.g., $\varphi \geq 135^\circ$, whereas they are comparable for smaller incident angles. Such changes in spectral shape
 307 may be associated with the strength of current effects on waves of various lengths (group speed) and directions.
 308 Nevertheless, it should be noted that both the Type-I and II WCI can modify the spectral shapes by generating a
 309 transfer of energy towards high wavenumbers (refer to the linear current-modified wave spectra (Figure 7 in
 310 Wang, et al. (2021))). These evident changes in spectra should be attributed to the nonlinear wave-wave
 311 interactions since they are also observed even without the presence of current. Meanwhile, the obtained
 312 simulation results hereby address that the Type-I WCI can further modify the spectral shapes on top of the
 313 modifications that are already incurred by the Type-II WCI, i.e., due to the nonlinear effects of the current.
 314 However, a comprehensive study on a wider variety of wave and current conditions is needed to further
 315 investigate and verify this phenomenon, which however is beyond the scope of this paper.



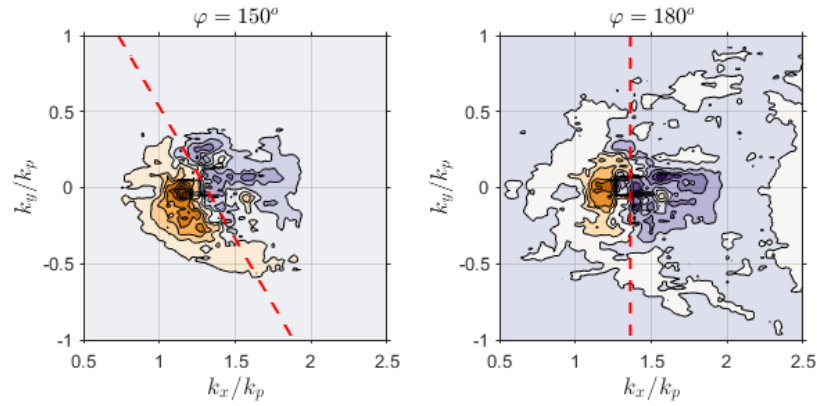
316

317

(a) $\varphi = 90^\circ$

(b) $\varphi = 110^\circ$

(c) $\varphi = 135^\circ$



318

319

(d) $\varphi = 150^\circ$

(e) $\varphi = 180^\circ$

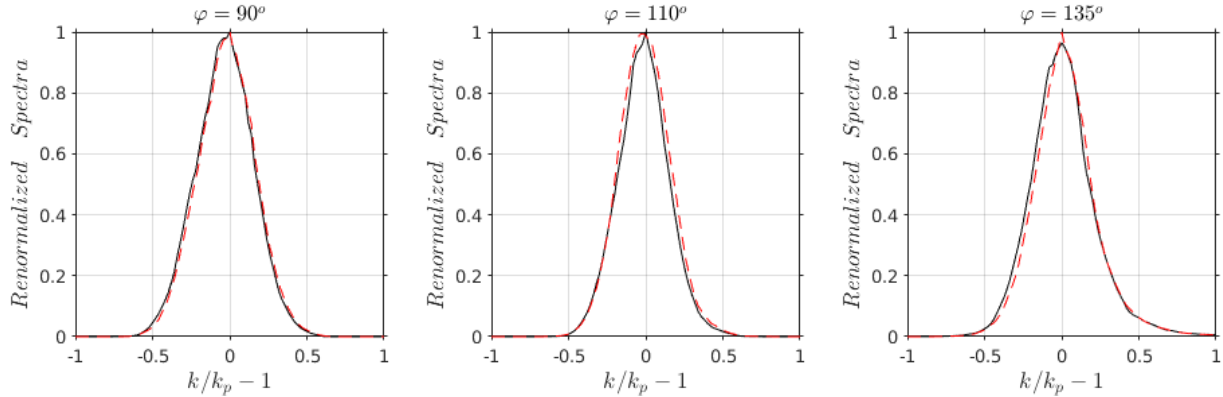
320

Figure 8. Values of R_s with respect to different current incident angles. Red dash line denotes the position of

321

divider line (Eq.(12)).

322



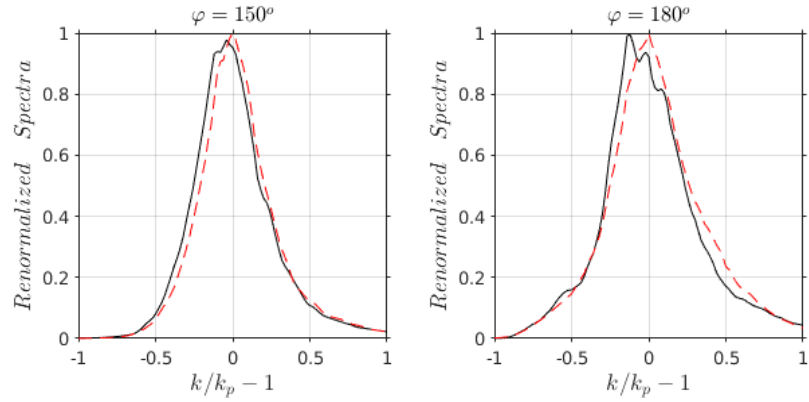
323

(a) $\varphi = 90^\circ$

(b) $\varphi = 110^\circ$

(c) $\varphi = 135^\circ$

324



(d) $\varphi = 150^\circ$

(e) $\varphi = 180^\circ$

Figure 9. Cross-sectional spectrum profiles along the line markers in Figure 7 perpendicular to those in Figure

8. Black solid line: Group (I); Red dash line: Group (II).

3.2.2 Spectral peak downshift

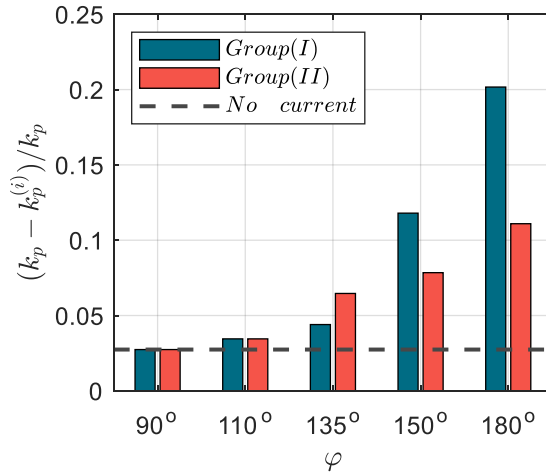
In addition to modifying the spectral shapes, it is shown that the presence of current can affect the downshift of the spectral peak (Wang, et al., 2021). According to Eq.(7), the oblique and opposed current can compress the wavelength leading to enlarged peak wavenumber. For a non-zero current speed, when the current incident angle φ increases, the peak wavenumber will shift to the higher end leading to shorter wave appearances. However, Eq.(7) only applies to small steepness waves, the actual spectral peak will be downshifted due to nonlinear quasi-resonant wave-wave interactions (Janssen, 2003).

To quantify the downshift of spectral peak and identify the role of nonlinear wave-current interactions, we employ the formula:

$$R_{kp} = \frac{k_p - k_p^{(i)}}{k_p} \quad (13)$$

339 where $k_p^{(i)}$ is the peak wavenumber obtained from the simulated spectra, and $i = \text{I or II}$ corresponds to Group
340 (I) or (II), respectively. The downshift is denoted by positive R_{kp} , and larger value indicates stronger downshift
341 effects. The values of R_{kp} are summarized and displayed in Figure 10. It shows that the downshift of spectral
342 peak becomes more evident with the increase of current incident angle. For $\varphi = 180^\circ$, the downshift can reach
343 20% when considering the nonlinear wave-wave and wave-current interactions simultaneously (Type-I WCI).
344 By comparing the results between the two groups, it is noted that at small incident angles, i.e., $\varphi \leq 110^\circ$, the
345 Type-I WCI has negligible effects on the downshift. At the angle of $\varphi = 90^\circ$, the downshift of spectral peak is
346 identical between the two groups and equals to the scenario without the current. However, the Type-I WCI can
347 enhance the downshift at relatively large angles, e.g., $\varphi \geq 150^\circ$. For instance, at the angle $\varphi = 180^\circ$, the
348 downshift can increase by 9% (from 11% for Group (II) to 20% for Group (I)). Nevertheless, it is noticed that
349 the Type-I WCI has reduced the downshift effects in the case for $\varphi = 135^\circ$. A comprehensive study should be
350 conducted to consider more current incident angles, so that this transition from reduction to enhancement of
351 spectral peak downshift can be investigated.

352 To summarize, the Type-I WCI can further change the spectral shapes at all current incident angles being
353 considered in this study. It is found to transfer energy from one part of the spectrum to the other part, and the
354 two parts are divided by a straight line across the spectral peak with the slope associated with the current incident
355 angle. Meanwhile, the Type-I WCI can further enhance the spectral peak downshift but only for angle $\varphi \geq 135^\circ$.
356 For opposed current, i.e., $\varphi = 180^\circ$, the downshift is further enhanced by 9% compared with Type-II WCI.



357

358

Figure 10. Shifts of spectral peak versus current incident angles.

359 4 Conclusions

360

This study investigates the role of two types of wave-current interactions on the extreme wave probability and

361

wave spectral properties in directional seas with oblique and opposed current. A number of numerical simulations

362

on large spatiotemporal scale based on fully nonlinear potential theory are performed. The JONSWAP spectrum

363

with a fixed peak factor and directional spreading is used to generate the random waves. A variety of current

364

incident angles ranging from 90° to 180° are considered to represent different scenarios in reality. Two groups of

365

numerical simulations are carried out for comparisons. The first group considers the fully nonlinear wave-wave

366

and wave-current interactions simultaneously (Type-I wave-current interactions), while the other accounts for

367

compound fully nonlinear wave-wave interactions and linear wave-current interactions (Type-II wave-current

368

interactions).

369

The results show that the Type-I wave-current interactions can further enhance the wave crest exceedance

370 probability at the distribution tail when compared with Type-II wave-current interactions. The enhancement
371 reaches the maxima at current incident angle of $110^\circ \sim 135^\circ$, whereas the effects become negligible when the
372 current is perpendicular or opposed to the mean wave direction. Meanwhile, the Type-I wave-current interactions
373 is found to have more significant impacts on the spectral shape and downshift of the spectral peak. It is noted
374 that each spectrum features two sub-regions that behave quite differently. Each sub-region subject to either gain
375 or loss of energy depending on the side of the divider, which is a straight line across the spectral peak with the
376 slope associated with the current incident angle. Besides, the Type-I wave-current interactions can further modify
377 the downshift of the spectral peak, but only for large current incident angle ($\varphi \geq 135^\circ$). For angle greater than
378 150° , downshift is enhanced due to the Type-I wave-current interactions, whereas for $\varphi = 135^\circ$, they will reduce
379 the downshift. The Type-I wave-current interactions has marginal effects on spectral peak downshift when $\varphi \leq$
380 110° .

381 Therefore, it can be concluded that the variations are evident in extreme wave probability and spectral properties
382 induced by the two different mechanisms, namely, the fully nonlinear wave-current interactions and composite
383 linear wave-current and fully nonlinear wave-wave interactions. Nevertheless, the limitation of this study is that
384 only the JONSWAP spectrum with fixed bandwidth and spreading is employed. Further investigations should be
385 conducted to examine the sensitivity of the results on different types of input spectra. Hence, the conclusions
386 drawn in this study are not directly transferable to other cases beyond the selected wave and current conditions,
387 though they are representative and quite typical in reality. In addition, a more comprehensive study with a wider
388 variety of wave and current conditions is also worthwhile in order to investigate i) the gain and loss of energy in
389 different quadrant of the spectrum domain, and ii) the transition from reduction to enhancement on the spectral

390 peak downshift within $\varphi = 135^\circ \sim 150^\circ$.

391 **Acknowledgements**

392 The first author shows gratitude to the sponsorship provided by PolyU-UGC, Hong Kong (P0039692). The
 393 second author gratefully acknowledge the financial support of EPSRC, UK (EP/V040235/1,
 394 EP/T00424X/1).

395

396 **Appendix**

397 The formulations of the fully nonlinear wave-wave interaction terms Φ and Ψ are given as

$$\Phi = F\{V\} - KF\{\tilde{\phi}\} \quad (\text{A. 1})$$

$$\Psi = \frac{1}{2}F \left\{ \frac{(V + \nabla\zeta \cdot \nabla\tilde{\phi})^2}{1 + |\nabla\zeta|^2} - |\nabla\tilde{\phi}|^2 \right\} \quad (\text{A. 2})$$

398 In addition, the vertical velocity $V = \sum_{i=1}^4 V_i$ and each part can be calculated by using

$$V_1 = F^{-1}\{KF\{\tilde{\phi}\}\} \quad (\text{A. 3})$$

$$V_2 = -F^{-1}\{KF\{\zeta V_1\}\} - \nabla \cdot (\zeta \nabla \tilde{\phi}) \quad (\text{A. 4})$$

$$V_3 = F^{-1} \left\{ \frac{K}{2\pi} F \left\{ \int \tilde{\phi}' \left[1 - \frac{1}{(1 + D^2)^{3/2}} \right] \nabla' \cdot \left[(\zeta' - \zeta) \nabla' \frac{1}{R} \right] d\mathbf{X}' \right\} \right\} \quad (\text{A. 5})$$

$$V_4 = F^{-1} \left\{ \frac{K}{2\pi} F \left\{ \int \frac{V'}{R} \left(1 - \frac{1}{\sqrt{1+D^2}} \right) d\mathbf{X}' \right\} \right\} \quad (\text{A. 6})$$

399 where $D = (\zeta' - \zeta)/R$, $R = |\mathbf{R}| = |\mathbf{X}' - \mathbf{X}|$, the variables with the prime indicate those at source point
400 (\mathbf{X}', Z') , the variables without the prime are those at field point (\mathbf{X}, Z) . Note that V_3 and V_4 can be further
401 written into convolutions up to seventh order, i.e.,

$$V_3 = \underbrace{V_3^{(1)}}_{4th \text{ convolution}} + \underbrace{V_3^{(2)}}_{6th \text{ convolution}} + \underbrace{V_{3,I}}_{\text{integration}} \quad (\text{A. 7})$$

$$V_4 = \underbrace{V_4^{(1)}}_{3rd \text{ convolution}} + \underbrace{V_4^{(2)}}_{5th \text{ convolution}} + \underbrace{V_4^{(3)}}_{7th \text{ convolution}} + \underbrace{V_{4,I}}_{\text{integration}} \quad (\text{A. 8})$$

402 where the convolution parts of V_3 are given by

$$F \{V_3^{(1)}\} = -\frac{K}{6} \left[Ki\mathbf{K} \cdot F\{\zeta^3 \nabla \tilde{\phi}\} - 3F \left\{ \zeta F^{-1} \left\{ Ki\mathbf{K} \cdot F\{\zeta^2 \nabla \tilde{\phi}\} \right\} \right\} \right. \\ \left. + 3F \left\{ \zeta^2 F^{-1} \left\{ Ki\mathbf{K} \cdot F\{\zeta \nabla \tilde{\phi}\} \right\} \right\} + F \left\{ \zeta^3 F^{-1} \left\{ K^3 F\{\tilde{\phi}\} \right\} \right\} \right] \quad (\text{A. 9})$$

$$F \{V_3^{(2)}\} = -\frac{K}{120} \left[i\mathbf{K}K^3 \cdot F\{\zeta^5 \nabla \tilde{\phi}\} - 5F \left\{ \zeta F^{-1} \left\{ i\mathbf{K}K^3 \cdot F\{\zeta^4 \nabla \tilde{\phi}\} \right\} \right\} \right. \\ \left. + 10F \left\{ \zeta^2 F^{-1} \left\{ i\mathbf{K}K^3 \cdot F\{\zeta^3 \nabla \tilde{\phi}\} \right\} \right\} - 10F \left\{ \zeta^3 F^{-1} \left\{ i\mathbf{K}K^3 \cdot F\{\zeta^2 \nabla \tilde{\phi}\} \right\} \right\} \right. \\ \left. + 5F \left\{ \zeta^4 F^{-1} \left\{ i\mathbf{K}K^3 \cdot F\{\zeta \nabla \tilde{\phi}\} \right\} \right\} + F \left\{ \zeta^5 F^{-1} \left\{ K^5 F\{\tilde{\phi}\} \right\} \right\} \right] \quad (\text{A. 10})$$

403 and the integration part

$$F \{V_{3,I}\} = \frac{K}{2\pi} F \left\{ \frac{35}{16} \int \tilde{\phi}' \nabla' \cdot \left[(\zeta' - \zeta) \nabla' \frac{1}{R} \right] D^6 d\mathbf{X}' \right. \\ \left. + \int \tilde{\phi}' \left[1 - (1 + D^2)^{-3/2} - \frac{3}{2} D^2 + \frac{15}{8} D^4 - \frac{35}{16} D^6 \right] \nabla' \right. \\ \left. \cdot \left[(\zeta' - \zeta) \nabla' \frac{1}{R} \right] d\mathbf{X}' \right\} \quad (\text{A. 11})$$

404 Meanwhile, the convolution parts of V_4 are given by

$$F\{V_4^{(1)}\} = -\frac{K}{2}\left[KF\{\zeta^2V\} - 2F\{\zeta F^{-1}\{KF\{\zeta V\}\}\} + F\{\zeta^2 F^{-1}\{KF\{V\}\}\}\right] \quad (\text{A. 12})$$

$$F\{V_4^{(2)}\} = -\frac{K}{24}\left[K^3F\{V\zeta^4\} - 4F\{\zeta F^{-1}\{K^3F\{V\zeta^3\}\}\} + 6F\{\zeta^2 F^{-1}\{K^3F\{V\zeta^2\}\}\}\right. \\ \left. - 4F\{\zeta^3 F^{-1}\{K^3F\{V\zeta\}\}\} + F\{\zeta^4 F^{-1}\{K^3F\{V\}\}\}\right] \quad (\text{A. 13})$$

$$F\{V_4^{(3)}\} = \frac{-K}{720}\left[K^5F\{V\zeta^6\} - 6F\{\zeta F^{-1}\{K^5F\{V\zeta^5\}\}\} + 15F\{\zeta^2 F^{-1}\{K^5F\{V\zeta^4\}\}\}\right. \\ \left. - 20F\{\zeta^3 F^{-1}\{K^5F\{V\zeta^3\}\}\} + 15F\{\zeta^4 F^{-1}\{K^5F\{V\zeta^2\}\}\}\right. \\ \left. - 6F\{\zeta^5 F^{-1}\{K^5F\{V\zeta\}\}\} + F\{\zeta^6 F^{-1}\{K^5F\{V\}\}\}\right] \quad (\text{A. 14})$$

405 and the integration part

$$F\{V_{4,I}\} = \frac{K}{2\pi}F\left\{\int \frac{V'}{R}\left(1 - \frac{1}{\sqrt{1+D^2}} - \frac{1}{2}D^2 + \frac{3}{8}D^4 - \frac{5}{16}D^6\right)d\mathbf{X}'\right\} \quad (\text{A. 15})$$

406 The integration terms are insignificant thus can be neglected when the wave steepness is small but will be

407 included in the calculation automatically when wave steepness becomes sufficiently large.

408 On the other hand, the formulations representing the fully nonlinear wave-current interactions can be given as

$$\begin{pmatrix} \mu \\ \psi \end{pmatrix} = \begin{pmatrix} F\{\nabla\eta \cdot \mathbf{U} + \eta(\nabla \cdot \mathbf{U})\} \\ F\{\nabla\tilde{\phi} \cdot \mathbf{U} - \eta(\nabla\tilde{\eta} \cdot \mathbf{U})\nabla \cdot \mathbf{U} + \frac{1}{2}(\eta\nabla \cdot \mathbf{U})^2\} \end{pmatrix} \quad (\text{A. 16})$$

409

410 **References**

411 Adcock, T. A. A. & Taylor, P. H., 2014. The physics of anomalous ('rogue') ocean waves. *Reports on Progress*

412 *in Physics*, 77(10), p. 105901.

413 Bakhanov, V. V. et al., 1996. *Evolution of surface waves of finite amplitude in field of inhomogeneous current.*
414 Lincoln, USA, International Geoscience and Remote Sensing Symposium (Vol. 1, pp. 609-611).

415 Benetazzo, A. et al., 2017. On the shape and likelihood of oceanic rogue waves. *Scientific Reports*, 7(1), p. 8276.

416 Cattrell, A. D., Srokosz, M., Moat, B. I. & Marsh, R., 2018. Can rogue waves be predicted using characteristic
417 wave parameters?. *Journal of Geophysical Research: Oceans*, Volume 123, pp. 1-13.

418 Choi, W., 2009. Nonlinear surface waves interacting with a linear shear current. *Mathematics and Computers in*
419 *Simulation*, 80(1), pp. 29-36.

420 Dysthe, K., Krogstad, H. E. & Müller, P., 2008. Oceanic rogue waves. *Annu. Rev. Fluid Mech.*, Volume 40, pp.
421 287-310.

422 ECMWF, 2018. *Sea level daily gridded data from satellite observations for the global ocean from 1993 to present.*
423 [Online]
424 Available at: <https://cds.climate.copernicus.eu/cdsapp#!/dataset/satellite-sea-level-global?tab=overview>
425 [Accessed 28 4 2022].

426 Fadaeiazar, E. et al., 2020. Fourier amplitude distribution and intermittency in mechanically generated surface
427 gravity waves. *Physical Review E*, 102(1), p. 013106.

428 Fang, W., Guo, Z. & Huang, Y., 1998. Observational study of the circulation in the southern South China Sea.
429 *Chinese Science Bulletin*, 43(11), pp. 898-905.

430 Fedele, F., 2015. On the kurtosis of deep-water gravity waves. *Journal of Fluid Mechanics*, Volume 782, pp. 25-

431 36.

432 Fedele, F. et al., 2016. Real world ocean rogue waves explained without the modulational instability. *Scientific*
433 *reports*, Volume 6, p. 27715.

434 Goda, Y., 1999. A Comparative Review on the Functional Forms of Directional Wave Spectrum. *Coastal*
435 *Engineering Journal*, 41(1), pp. 1-20.

436 Guyenne, P., 2017. A high-order spectral method for nonlinear water waves in the presence of a linear shear
437 current. *Computers & Fluids*, Volume 154, pp. 224-235.

438 Huang, N. E., Chen, D. T., Tung, C. C. & Smith, J. R., 1972. Interactions between steady non-uniform currents
439 and gravity waves with applications for current measurements. *Journal of Physical Oceanography*, 2(4), pp.
440 420-431.

441 Janssen, P. A., 2003. Nonlinear four-wave interactions and freak waves. *Journal of Physical Oceanography*,
442 33(4), pp. 863-884.

443 Janssen, P. A., 2009. On some consequences of the canonical transformation in the Hamiltonian theory of water
444 waves. *Journal of Fluid Mechanics*, Volume 637, pp. 1-44.

445 Janssen, P. A. & Bidlot, J. R., 2009. *On the extension of the freak wave warning system and its verification*,
446 Reading, England: European Centre for Medium-Range Weather Forecasts.

447 Janssen, T. T. & Herbers, T. H. C., 2009. Nonlinear wave statistics in a focal zone. *Journal of Physical*
448 *Oceanography*, 39(8), pp. 1948-1964.

449 Kharif, C., Abid, M. & Touboul, J., 2017. Rogue waves in shallow water in the presence of a vertically sheared
450 current. *Journal of Ocean Engineering and Marine Energy*, 3(4), pp. 301-308.

451 Kharif, C., Pelinovsky, E. & Slunyaev, A., 2009. *Rogue Waves in the Ocean*. Berlin Heidelberg: Springer-Verlag.

452 Lavrenov, I. V., 1998. The wave energy concentration at the Agulhas current off South Africa. *Natural hazards* ,
453 17(2), pp. 117-127.

454 Lavrenov, I. V., 2003. *Wind-Waves in Oceans: Dynamics and Numerical Simulations*. Berlin: Springer.

455 Lavrenov, I. V. & Porubov, A. V., 2006. Three reasons for freak wave generation in the non-uniform current.
456 *European Journal of Mechanics-B/Fluids*, 25(5), pp. 574-585.

457 Liao, B., Dong, G., Ma, Y. & Gao, J. L., 2017. Linear-shear-current modified Schrödinger equation for gravity
458 waves in finite water depth. *Physical Review E*, 96(4), p. 043111.

459 Li, J., Chen, Y. & Pan, S., 2016. Modelling of extreme wave climate in China Seas. *Journal of Coastal Research*,
460 75(sp1), pp. 522-526.

461 Longuet-Higgins, M. S. & Stewart, R. W., 1961. The changes in amplitude of short gravity waves on steady non-
462 uniform currents. *Journal of Fluid Mechanics*, 10(4), pp. 529-549.

463 Lyard, F. H. et al., 2021. FES2014 global ocean tide atlas: design and performance. *Ocean Science*, 17(3), pp.
464 615-649.

465 Manolidis, M., Orzech, M. & Simeonov, J., 2019. Rogue Wave Formation in Adverse Ocean Current Gradients.
466 *Journal of Marine Science and Engineering*, 7(2), p. 26.

467 Ma, Y., Ma, X., Perlin, M. & Dong, G., 2013. Extreme waves generated by modulational instability on adverse
468 currents. *Physics of Fluids*, Volume 25, p. 114109.

469 Moreira, R. M. & Peregrine, D. H., 2012. Nonlinear interactions between deep-water waves and currents.
470 *Journal of Fluid Mechanics*, Volume 691, pp. 1-25.

471 Mori, N. & Janssen, P. A., 2006. On kurtosis and occurrence probability of freak waves. *Journal of Physical*
472 *Oceanography*, 36(7), pp. 1471-1483.

473 Nwogu, O., 2009. Interaction of finite-amplitude waves with vertically sheared current fields. *Journal of fluid*
474 *mechanics*, Volume 627, pp. 179-213.

475 Onorato, M., Osborne, A. R. & Serio, M., 2008. *On deviations from Gaussian statistics for surface gravity waves*.
476 Manoa, Honolulu, US, In Proceedings of the Hawaiian Winter Workshop, University of Hawaii.

477 Peregrine, D. H., 1976. Interaction of water waves and currents. *Advances in applied mechanics*, Volume 16, pp.
478 9-117.

479 Ruban, V., 2012. On the nonlinear Schrödinger equation for waves on a nonuniform current. *JETP Letter*, Volume
480 95, p. 486–491.

481 Stocker, J. R. & Peregrine, D. H., 1999. The current-modified nonlinear Schrödinger equation. *Journal of Fluid*
482 *Mechanics*, Volume 399, pp. 335-353.

483 Tayfun, M. & Fedele, F., 2007. Wave-height distributions and nonlinear effects. *Ocean engineering*, 34(11-12),
484 pp. 1631-1649.

485 Thomas, R., Kharif, C. & Manna, M., 2012. A nonlinear Schrödinger equation for water waves on finite depth
486 with constant vorticity. *Physics of fluids*, 24(12), p. 127102.

487 Toffoli, A. et al., 2011. Occurrence of extreme waves in three-dimensional mechanically generated wave fields
488 propagating over an oblique current. *Natural Hazards and Earth System Sciences*, 11(3), pp. 895-903.

489 Toffoli, A. et al., 2015. Rogue waves in opposing currents: an experimental study on deterministic and stochastic
490 wave trains. *Journal of Fluid Mechanics*, Volume 769, pp. 277-297.

491 Touboul, J. & Kharif, C., 2016. Effect of vorticity on the generation of rogue waves due to dispersive focusing.
492 *Natural Hazards*, 84(2), pp. 585-598.

493 Trulsen, K. et al., 2015. Crossing sea state and rogue wave probability during the Prestige accident. *J. Geophys.*
494 *Res. Oceans*, Volume 120, p. 7113– 7136.

495 Wang, J. & Ma, Q. W., 2015. Numerical techniques on improving computational efficiency of Spectral Boundary
496 Integral Method. *International Journal for Numerical Methods in Engineering*, 102(10), pp. 1638-1669.

497 Wang, J., Ma, Q. W. & Yan, S., 2018. A fully nonlinear numerical method for modeling wave–current interactions.
498 *Journal of Computational Physics*, Volume 369, pp. 173-190.

499 Wang, J., Ma, Q. W. & Yan, S., 2021. On Extreme Waves in Directional Seas with Presence of Oblique Current.
500 *Applied Ocean Research*, Volume 112, p. 102586.

501 Wang, J., Ma, Q. W., Yan, S. & Liang, B., 2021. Modeling Crossing Random Seas by Fully Non-Linear
502 Numerical Simulations. *Frontiers in Physics*, Volume 9, p. 188.

503 Waseda, T., Kinoshita, T., Cavaleri, L. & Toffoli, A., 2015. Third-order resonant wave interactions under the
504 influence of background current fields. *Journal of Fluid Mechanics*, Volume 784, pp. 51-73.

505 White, B. S. & Fornberg, B., 1998. On the chance of freak waves at sea. *Journal of fluid mechanics*, Volume
506 355, pp. 113-138.

507 Xiao, W., Liu, Y., Wu, G. & Yue, D. K. P., 2013. Rogue wave occurrence and dynamics by direct simulations of
508 nonlinear wave-field evolution. *Journal of Fluid Mechanics*, Volume 720, pp. 357-392.

509

510